Conduction-electron scattering in quenched and annealed gold*

Y. K. Chang[†] and G. W. Crabtree

Argonne National Laboratory, Argonne, Illinois 60439

J. B. Ketterson

Department of Physics and Materials Research Center, Northwestern University, Evanston, Illinois 60201
and Argonne National Laboratory, Argonne, Illinois 60439

(Received 18 February 1977)

The anisotropy of the conduction-electron scattering due to vacancies and stacking-fault tetrahedra (SFT) in quenched and subsequently annealed gold single crystals has been studied by measuring the de Haas–van Alphen (dHvA) Dingle (scattering) temperatures T_D for a large number of cyclotron orbits. The samples were quenched from 900°C into ice water, and were later annealed at 23 and 40°C. We find that the dHvA scattering rates $1/\tau_{dHvA}$ due to both vacancies and SFT are much larger than those obtained from resistivity measurements $1/\tau_\rho$. The ratio of the [111] neck to belly orbital scattering rate rises from 1.0 for vacancies to 3.5 for SFT. This is attributed to the stronger and longer range strain field associated with the larger defects. We have calculated the local lifetimes $\tau(\vec{k})$ from the measured T_D and found a large scattering anisotropy with the strongest scattering arising from the [100] region.

I. INTRODUCTION

Vacancies and their clusters in gold have been studied extensively in the past two decades. The initial vacancy distribution is usually produced by quenching. In this process a vacancy distribution in equilibrium at high temperatures is frozen in place by rapid cooling to a temperature at which the vacancies are no longer mobile. Upon annealing at room temperature or above, the vacancies begin to migrate and form large clusters. These defects have been studied by resistivity measurements,[1] transmission electron microscopy,[2-5] and, recently, by the positron annihilation technique.[6] Strong direct evidence has shown that, during the annealing, the vacancies aggregate into stacking-fault tetrahedra[2,4,5] (SFT). Each stacking-fault tetrahedron is bounded by four {111} stacking faults intersecting each other with ⟨110⟩ stair-rod dislocations. Most of these studies have been carried out in polycrystalline gold which usually contains a high density of dislocations and many grain boundaries, which can act as effective vacancy sinks. This is demonstrated by the bending over of the Arrhenius plot at high quenching temperatures. With carefully prepared gold single crystals, Lengeler[7] obtained a straight Arrhenius plot, and showed that the dislocations are the dominant sinks for vacancies.

The de Haas–van Alphen (dHvA) effect[8] has been successfully used for studying the electron-impurity interaction in dilute alloys[9] as well as for obtaining accurate information about the Fermi-surface geometry of metals. Owing to its sensitivity to the small-angle scattering arising from

the defect strain field, the dHvA effect is a potential tool for studying structural defect scattering. In this respect the dHvA effect is complementary to the usual resistivity measurements, which are much more sensitive to the large-angle scattering from the defect itself. Defects studied by dHvA techniques include edge dislocations,[10-12] dislocation loops in copper,[13] and vacancies in gold.[14-16] Since the dHvA effect arises from a well-defined group of electrons on the Fermi surface, it can provide detailed information about the interaction of conduction electrons with defects.

In this paper we extend our earlier work[14] on vacancies in quenched Au and report new data on SFT formed by annealing the same quenched samples. These defect systems were chosen because they are relatively simple, well characterized, and have been extensively studied by other techniques. In particular, vacancies are point defects with high symmetry which also induce significant lattice distortion. They are a natural intermediate case between substitutional impurities, which produce relatively little lattice strain, and extended defects like dislocations and SFT where the associated strain field is a major feature of the defect. The Dingle temperature T_D is related to orbital scattering lifetime τ through $T_D = (\hbar/2\pi k_B)(1/\tau)$. The values of T_D were measured for as many as thirty cyclotron orbits in one sample. The local lifetime, $\tau(\vec{k})$, for each state on the Fermi surface was inferred using a Fourier series expansion of Fermi-surface properties. "Lifetime maps" of the basic $\frac{1}{48}$ of the Brillouin zone are presented for vacancies and SFT. A brief version of this work was given elsewhere.[15]

II. EXPERIMENTAL

The de Haas–van Alphen effect was detected by the field-modulation technique.[17-19] The experimental system consisted of a 75 kG superconducting magnet with an axial field homogeneity of 1 part in 10^5 over a 2-mm region at the center of the magnet. Samples could be rotated in any crystallographic plane; the initial alignment was achieved using x-ray techniques.[19] The system employed an on-line PDP-11 minicomputer with software for performing fast and slow Fourier transforms. An associated disk system permitted data storage and retrieval. Gold wires of 0.75-mm diameter and 99.999% purity were obtained from Sigmund Cohn Mfg. Co. (Mount Vernon, N.Y.). The polycrystalline wires were etched in aqua regia and dried with methanol. Single crystals were grown using the floating-zone technique at a rate of about 5 cm/h; precautions were taken to keep the system free from contamination. The dHvA samples were cut slightly oversized and were etched in aqua regia to fit smoothly into the dHvA sample holder. Typically, the samples were 0.63 mm in diameter and 1 mm long.

All samples were annealed in air in a tubular resistance furnace at 900 °C for 16 h to increase the residual-resistivity ratio and reduce possible strain. Samples prepared in this way had residual-resistivity ratios greater than 2000. Quenching was done by heating the sample in a large ceramic boat in the furnace at the desired quenching temperature for approximately 30 min. The sample and boat were quickly pulled out of the furnace opening, and the sample was dumped into an ice-water quenching bath located at the edge of the furnace opening. The large heat capacity of the boat coupled with the quick release of the sample just above the liquid level minimized precooling prior to the sample's entrance into the quenching bath. The sample fell through ice water for a distance of ~5 cm before coming to rest on a soft bottom.

To check our quenching procedure, we treated a series of polycrystalline wires of about 0.7 mm diameter by 8 mm long with the above annealing and quenching procedures. Five samples were quenched from several temperatures between 700 and 1000 °C. As can be seen from Fig. 1, the initial quenched-in resistivities $\Delta\rho_0$ formed a smooth Arrhenius plot with values higher than those found for polycrystals, but comparable to those reported for single crystals.[7] The higher values reported here may be due to the use of a short sample length, which is essential for obtaining uniform quenching and minimizing strain.[20] In addition, our annealing and quenching procedures differ
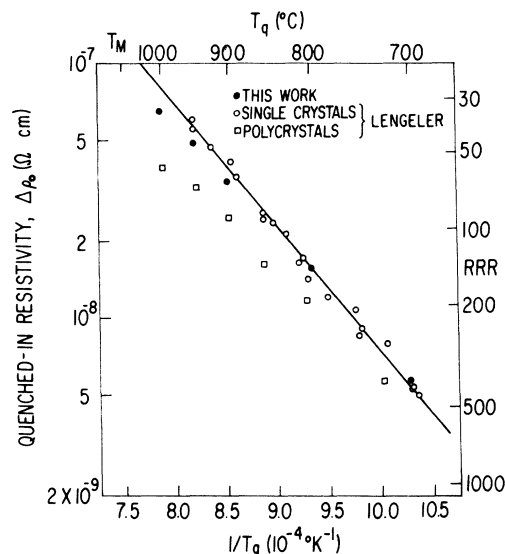

FIG. 1. Initial quenched-in resistivity $\Delta\rho_0$ as a function of the quenching temperature T_q, obtained by quenching a series of well-annealed gold polycrystalline wires. Data from Ref. 7 are also shown. Shown on the right is the residual-resistivity ratio (RRR), defined as $\rho_{23°C}/\rho_{4.2°K}$, where $\rho_{23°C}$ is taken to be 2.23 $\mu\Omega$ cm.

somewhat from those used earlier. The smooth Arrhenius plot, in satisfactory agreement with earlier results, indicates that our sample handling and quenching techniques are sound. We expect the quenched-in resistivities of the single-crystal samples, which were too small for direct resistivity measurement, to be comparable with those shown in Fig. 1.

We also measured the residual resistivity $\Delta\rho(t)$ as a function of isothermal (room-temperature) annealing time for polycrystalline samples quenched from different temperatures. The results (Fig. 2) showed that the resistivity in samples quenched from high temperatures dropped faster, but retained a higher final value than in
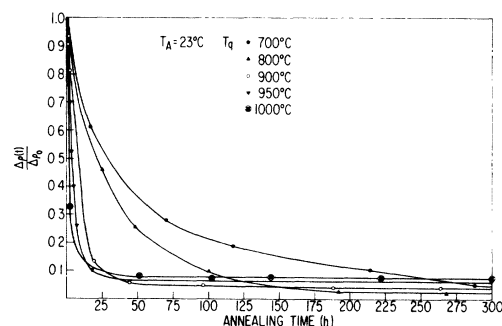

FIG. 2. Fractional residual resistivity as a function of isothermal (at 23 °C) annealing time for those gold wires used in Fig. 1.

samples quenched from lower temperatures.
These results are consistent with those reported
elsewhere.[1,21] For samples quenched from 900 °C,
the final residual resistivity dropped to only 4% of
its initial value.

Two dHvA samples, Au1 and Au2, cut from dif-
ferent single crystals, were quenched from 900 °C
into ice water. Based on Fig. 1, the quenched-in
resistivity is estimated to be about 35 nΩ cm, cor-
responding to a vacancy concentration of 220 ppm.
After quenching, samples were quickly dried with
methanol and later handled at about ~-30 °C to pre-
vent migration of the vacancies before the dHvA
measurements were made.

III. EXPERIMENTAL RESULTS

The background Dingle temperatures of an un-
quenched sample cut from the same single crystal
as Au2 were measured over a number of cyclotron
orbits in a separate conduction-electron-g-factor
study.[22] The observed T_D for the belly orbits near
$\langle 111 \rangle$ were found to be ≤ 0.2 K; all other orbits
showed $T_D \leq 0.1$ K. Further checks on the quality
of the samples were provided by field rotation
data. Mosaic structure or strain[12,23,24] can pro-
duce a severe reduction of the off-symmetry dHvA
amplitudes or a beating effect in rotation curves.
All observed orbits were examined in field rota-
tion for all dHvA samples and no evidence of mo-
saic structure or strain was seen. These results
indicate that the purity and perfection of the sam-
ples were satisfactory.

The observed T_D on the quenched sample Au1
are shown as solid points in Fig. 3. Only a few
data points for bellies are shown for Au1 due to a
large rms error for belly orbits (arising from a
magnet power supply instability which was pre-
sent for that particular set of measurements). The
values for the [100] and [111] belly orbits shown
in Fig. 3 had standard deviations of ±0.08 °K com-
pared to ±0.02 °K for the other orbits. Off-sym-
metry bellies, in general, had large errors and
hence were not included in the figure. We repeated
the measurement (with improved field stability) on
another sample, Au2, which was treated in a met-
allurgically identical manner as Au1. The ob-
served T_D on this sample are shown as the solid
points in Fig. 4. These results are similar to
those of Au1. The orbital scattering anisotropy
is moderate with the variation in T_D less than 30%.
The dHvA scattering rate $(1/\tau)_{dH\,vA}$ is found to be at
least 50% stronger than the scattering rate $(1/\tau)_\rho$
estimated from the resistivity. This shows the
significance of the small-angle scattering caused
by the lattice distortion around a vacancy.

At a temperature near 0 °C or above, the vacan-
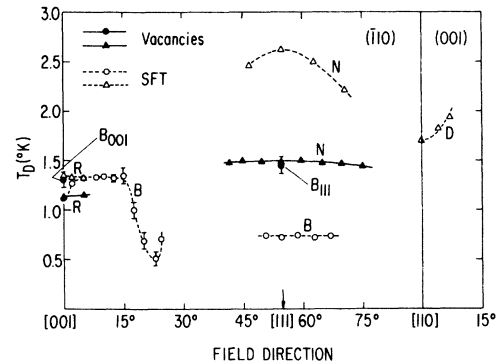cies in gold begin to migrate. Some of them may

FIG. 3. Dingle temperatures for both vacancies (solid
points) and stacking-fault tetrahedra (open points) mea-
sured in samples Au1 and Au1A, quenched from 900 °C
and subsequently annealed at 23 °C. Data for belly (B, in
circles), rosette (R), dogbone (D), and neck (N) orbits
are shown.

be trapped or annihilated at impurities, disloca-
tions, and grain boundaries. In a very pure and
nearly perfect single crystal, most of the vacan-
cies will aggregate to form SFT.[4,5] In gold, the
formation of SFT is favored over other defect clus-
ters, like dislocation loops, because the configura-
tion energy for SFT is lower.

The quenched sample Au1 was later aged at
room temperature (23 °C) for several months and
the quenched sample Au2 was annealed at 40 °C for
64h. (These samples will be denoted as Au1A and
Au2A, respectively.) These periods are sufficiently
long that the aggregation is complete, i.e., the re-
sidual resistivity is no longer time dependent. The
observed T_D in these two quenched and subsequent-
ly annealed gold samples are shown as open points
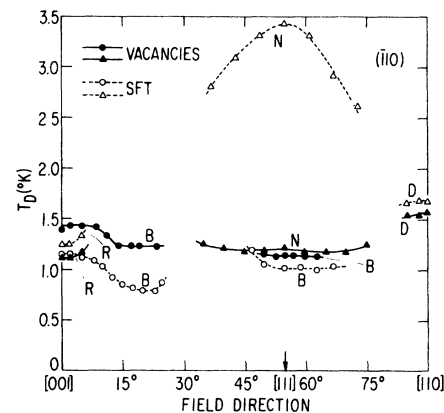in Figs. 3 and 4, respectively. Note that the final

FIG. 4. Dingle temperatures for both vacancies and
stacking-fault tetrahedra measured in samples Au2 and
Au2A, quenched from 900 °C and subsequently annealed at
40 °C. Same notation as that in Fig. 3 is used.

residual resistivity for an aged sample which was initially quenched from 900 °C, has dropped by a factor of 25 as shown in Fig. 2. In spite of this sharp decrease in resistivity, there is only a (10–30)% decrease in T_D for belly orbits and an approximate 10% increase for rosette and dogbone orbits. The greatest effect is for the neck, whose scattering rate *increases* by a factor of 3. We believe the difference in the behavior of resistivity and Dingle temperatures under annealing clearly demonstrates the influences of small-angle scattering due to the strain field surrounding the defects. For the dHvA effect, it is the strain field and not the defect itself which dominates the scattering lifetime. The ratio of the neck scattering rate $(1/\tau)_N$ to the belly scattering rate $(1/\tau)_B$ increases from about 1 for vacancies to 3.6 in Au1A and 3.4 in Au2A for SFT. This large scattering anisotropy is comparable to that observed for dislocations in copper[13]; this ratio is less than 1 for the dilute impurities in Au shown in Table IV.

There are also significant differences in T_D between Au1A and Au2A. The higher annealing temperature in Au2A (40 °C vs 23 °C for Au1A) is expected to produce SFT with longer edge lengths. Since both samples are expected to have the same number of quenched-in vacancies initially, Au2A would have fewer (but larger size) SFT. Figures 3 and 4 show that neck and belly T_D's in Au2A are higher than those in Au1A. Table I shows neck and belly Dingle temperatures at $\langle 111 \rangle$ for Au2A and Au1A. To compensate for any possible small differences in the quenched-in vacancy concentration, the ratio $T_D^{\text{SFT}}/T_D^{\text{vac}}$ is shown. For both neck and belly, there is more than 60% increase in scattering from larger SFT.

IV. DATA INVERSION

A. Fourier-series inversion scheme

Each quantity measured by the dHvA effect is an average of some point property of the Fermi surface over an extremal area cyclotron orbit. Where possible, it is more convenient to deal with the fundamental point properties of the Fermi surface itself. The measured orbital area A is related to $k_\perp$, the radius vector in the plane of the orbit,

TABLE I. Dingle temperatures for $\langle 111 \rangle$ neck and belly in annealed samples, normalized by corresponding Dingle temperatures in as-quenched samples.

	Belly	Neck
Au1A	0.49	1.76
Au2A	0.89	2.82

through

$$A = \frac{1}{2} \int_0^{2\pi} k_\perp^2 \, d\theta \; ;$$

the orbital effective mass m^* involves $k_\perp$ and $\vec{v}_F$, the Fermi velocity, through

$$m^* = \frac{\hbar}{2\pi} \int_0^{2\pi} \frac{k_\perp^2 \, d\theta}{\vec{v}_F \cdot \vec{k}_\perp} \; .$$

The orbital scattering rate $1/\tau$ may be expressed as an average over point (or local) scattering rates $1/\tau(\vec{k})$ using

$$\frac{1}{\tau} = \frac{\hbar}{2\pi m^*} \int_0^{2\pi} \frac{1}{\tau(\vec{k})} \frac{k_\perp^2 \, d\theta}{\vec{v}_F \cdot \vec{k}_\perp} \; . \tag{1}$$

In this expression the local scattering rate $1/\tau(\vec{k})$ is weighted by the time the electron spends at $\vec{k}$.

Two types of inversion schemes for finding point properties from orbital quantities have been proposed. In the first scheme, the quantity of interest is expanded in a set of functions which satisfy certain symmetry requirements. For example, for a closed single-valued surface with inversion symmetry, the problem of converting areas, masses, and orbital lifetimes into radii, velocities, and point lifetimes has been solved by expanding the data in appropriate spherical harmonics.[25-28] For an open surface the expansion is made in terms of a Fourier series which is invariant under the operations of the space group as well as the point group.[29-34] The second scheme employs the partial-wave scattering phase shifts η_l as adjustable parameters.[35-42] The latter scheme has the advantage of rapid convergence (hence, fewer parameters are needed), and that the phase shifts may have intrinsic physical meaning, in contrast to the nonphysical parameters used in the Fourier series or symmetrized spherical harmonic expansions. The partial-wave approach, based on the muffin-tin potential used in the Korringa-Kohn-Rostoker (KKR) method, neglects the lattice distortion in the neighborhood of a scattering center. Thus, from a fundamental point of view, this approach is not suitable for structural defects where there is significant lattice distortion (although it might still provide a usable parametrization). Therefore, we will adopt the Fourier-series technique in the present work to perform the local lifetime inversion.

An inversion scheme based on the Fourier series representation of the Fermi surface has already been used in noble metals[29,30]; an improved version has been discussed in detail elsewhere.[31,33] In this approach, the Fermi surface is represented by the implicit equation

$$F(\vec{k}, E) = \sum_{\mathbf{R}} C_{\vec{R}}(E) e^{i\vec{k} \cdot \vec{R}} = 0, \tag{2}$$

where $\vec{R}$ are the position vectors in a real-space Bravais lattice. If these vectors are factored into sets or "stars" which are invariant under point-group operations, Eq. (2) may be rewritten in the form

$$F(\vec{k}, E) = \sum_j C_j(E) S_j(\vec{k}),$$ (3)

where

$$S_j(\vec{k}) = \sum_{\vec{R} \text{ in } j\text{th star}} e^{i\vec{k}\cdot\vec{R}}.$$ (4)

Methods for obtaining the set of parameters C_j by a least-squares fit of the experimental cross-sectional areas have been described elsewhere.[31,33]

From the law of differentiation of an implicit function, we find the Fermi velocity as

$$\vec{v}_F = \frac{1}{\hbar}\vec{\nabla}E = -\frac{(1/\hbar)\vec{\nabla}F}{(\partial F/\partial E)_{\vec{k}}}, \quad \text{where } \vec{\nabla} \equiv \vec{\nabla}_k,$$ (5)

and Eq. (1) becomes

$$\frac{1}{\tau_i} = -\frac{\hbar^2}{2\pi m_i^*}\int_0^{2\pi}\frac{1}{\tau(\vec{k})}\left(\frac{\partial F}{\partial E}\right)_{\vec{k}}\frac{k_\perp^2}{\vec{k}_\perp\cdot\vec{\nabla}F}\,d\theta.$$ (6)

At this point there are two ways to proceed. In the first, described by Bosacchi et al.,[33,34] $(\partial F/\partial E)_{\vec{k}}$ is expanded as a Fourier series

$$\left(\frac{\partial F}{\partial E}\right)_{\vec{k}} = \sum_l C_l' S_l(\vec{k}),$$ (7)

where $C_l' \cong \partial C_l/\partial E$. Then Eq. (6) becomes

$$\frac{1}{\tau_i} = -\frac{\hbar^2}{2\pi m_i^*}\sum_l C_l'\int_0^{2\pi}\frac{k_\perp^2}{\vec{k}_\perp\cdot\vec{\nabla}F}S_l(\vec{k})\frac{d\theta}{\tau(\vec{k})}.$$ (8)

Expanding $1/\tau(\vec{k})$ in a Fourier series

$$\frac{1}{\tau(\vec{k})} = \sum_j f_j S_j(\vec{k}),$$ (9)

and, substituting in Eq. (8),

$$\frac{1}{\tau_i} = -\frac{\hbar^2}{2\pi m_i^*}\sum_{j,l} f_j C_l'$$

$$\times\int_0^{2\pi}\frac{k_\perp^2}{\vec{k}_\perp\cdot\vec{\nabla}F}S_l(\vec{k})S_j(\vec{k})\,d\theta.$$ (10)

Defining

$$X_j = -\frac{\hbar^2}{2\pi m_i^*}\sum_l C_l'$$

$$\times\int_0^{2\pi}\frac{k_\perp^2}{\vec{k}_\perp\cdot\vec{\nabla}F}S_l(\vec{k})S_j(\vec{k})\,d\theta$$ (11)

gives the relation

$$\frac{1}{\tau_i} = \sum_j f_j X_j.$$ (12)

In this scheme the coefficients C_j are determined by fitting a set of cross-sectional areas, the C_j' by fitting a set of effective masses, and the f_j by

fitting a set of orbital lifetimes. The local lifetime may then be computed from Eq. (9).

In the second scheme, which we present here for the first time, the quotient $(\partial F/\partial E)_{\vec{k}}/\tau(\vec{k})$ in Eq. (6) is expanded as a Fourier series:

$$\left(\frac{\partial F}{\partial E}\right)_{\vec{k}}\bigg/\tau(\vec{k}) = \sum_j f_j' S_j(\vec{k}).$$ (13)

Putting this into Eq. (6),

$$\frac{m_i^*}{\tau_i} = \frac{\hbar^2}{2\pi}\sum_j f_j'\frac{\partial A}{\partial C_j},$$ (14)

where

$$\frac{\partial A}{\partial C_j} = -\int_0^{2\pi}\frac{k_\perp^2}{\vec{k}_\perp\cdot\vec{\nabla}F}S_j(\vec{k})\,d\theta.$$

[In Eq. (11), X_j could also be defined without the factor m_i^* in which case one could also fit m_i^*/τ_i with the first method.] The quantities $\partial A/\partial C_j$ are available as a by-product of fitting the C_j to the area data; the f_j' are determined by fitting the ratio of mass to orbital lifetime. To compute local lifetimes, a set of C_j' must be determined by fitting effective masses. Then $\tau(\vec{k})$ is computed from Eq. (13)

$$\tau(\vec{k}) = \left(\frac{\partial F}{\partial E}\right)_{\vec{k}}\bigg/\sum_j f_j' S_j(\vec{k}) = \sum_j C_j' S_j(\vec{k})\bigg/\sum_j f_j' S_j(\vec{k}).$$ (15)

Note that the structure of Eq. (14) is very similar to the partial-wave phase-shift approach used by Coleridge et al.,[42] where $\partial A/\partial\eta_l$ plays the same role as $\partial A/\partial C_j$. The values $\partial A/\partial C_j$ for each cyclotron orbit depend only on the Fermi-surface geometry which can be inferred from experimental area data; the X_j involve the mass data. Lifetime coefficients, f_j or f_j', may be obtained by least-squares fitting equation (9) with lifetime data from the field-induced surface-state resonance effect,[43-45] or fitting Eq. (12) [or Eq. (14)] with experimental Dingle temperatures. The set of lifetime coefficients f_j or f_j' depending on the defect concentration and the approach used, are a representation of the local lifetime, since it allows one to calculate the local lifetimes from Eq. (9) [or Eq. (15)], and orbital lifetime from Eq. (12) [or Eq. (14)]. Which of the above techniques should be used depends on the relative convergence of each scheme which in turn depends on the nature of the anisotropy of $\tau(\vec{k})$. This can only be decided by examining the rms error for a given order of the expansion, the smaller rms deviation possibly providing the better representation.

B. Results of the inversion

The coefficients C_j and C_j' used in the present work to represent the Fermi surface of gold are

TABLE II. Values of coefficients C_j and C'_j used in the inversion.

C_j	$C'_j (\text{Ry}^{-1})$
1.000 000	0.000 00
4.028 360	0.000 00
−1.340 230	−82.458 60
−2.400 300	−70.848 50
−0.233 042	−16.891 50
−0.618 918	−14.724 80
0.118 184	12.108 80
0.198 816	6.958 52

taken from Ref. 33 and are given in Table II. We will employ a modified atomic unit, called the Brillouin unit, where the distance from Γ to X in the Brillouin zone of a fcc lattice is set equal to 1; in addition, all energies are measured in Ry. This means that all lengths in k space are in units of $2\pi/a$ (a is the lattice constant), which is 1.5456 $\times 10^8$ cm^{-1} for gold. The contour diagrams of calculated Fermi radius k_F, Fermi velocity v_F, and $|\vec{v}_F \cdot \hat{k}_F|$ using the sets of C_j and C'_j given in Table II are shown in Figs. 5–7. Due to the crystal symmetry, only $\frac{1}{48}$ of the Fermi surface is shown on a standard stereographic triangle.

The lifetime coefficients f'_j have been calculated by our second least-squares-fit procedure using the experimental Dingle temperatures given in Fig. 4 for vacancies and stacking-fault tetrahedra in Au1 and Au2A. The values of f'_j obtained from a five-term and a six-term fit are listed in Table III. For vacancies the rms error of the fit decreases slowly if the number of terms used in the fit is increased. However, it fails at eight
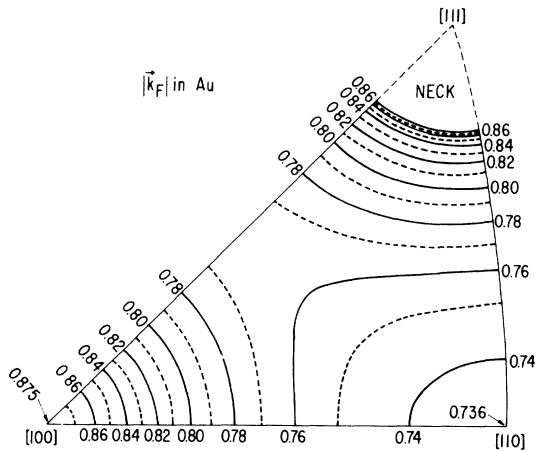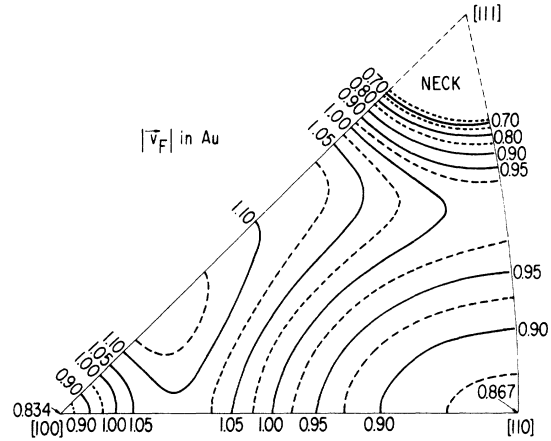

FIG. 6. Map of $|\vec{v}_F|$ shown in $\frac{1}{48}$ of the Fermi surface of gold. The numbers shown are in Brillouin units. To convert them to cgs units, those numbers should be multiplied by 1.3374×10^8 cm/sec.

terms due to a nearly singular behavior of the inversion matrix. The rms error of the fit for SFT is much higher, although it improves as the number of terms used in the fit is increased. The fit fails at seven terms for the same reason as the case of vacancies. The fact that the inversion matrix becomes singular with increasing number of terms arises partly from the fact that our expansion functions are not orthogonal when integrated over the surface (although they are, of course, orthogonal when integrated over the zone). Using a Schmidt-like procedure, surface orthogonal functions could be constructed and the singularity problem reduced.

The local lifetime map for vacancies in Au2 calculated from Eq. (15) using a six-term fit is shown in Fig. 8. The contour map calculated from the other procedure using Eq. (12) has been found to be nearly identical, and we will not discuss it further. Note that the variation in T_D for vacancies

FIG. 5. Map of $|\vec{k}_F|$ shown on $\frac{1}{48}$ of the Fermi surface of gold. The numbers shown are in Brillouin units, i.e., the distance Γ to X in the first Brillouin zone is set to 1. To convert them to cgs units, those numbers should be multiplied by 1.5456×10^8 cm^{-1}.
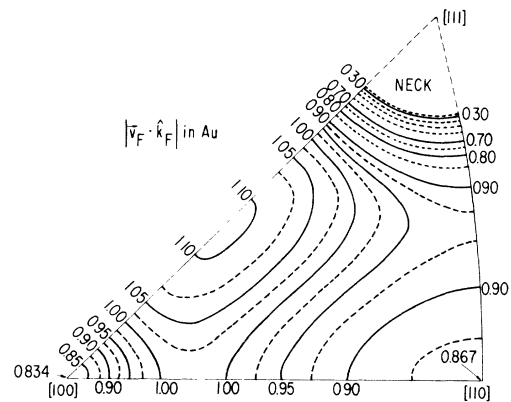

FIG. 7. Map of $|\vec{v}_F \cdot \hat{k}_F|$ shown on $\frac{1}{48}$ of the Fermi surface of gold. Same unit as in Fig. 6 is used.

TABLE III. Lifetime coefficients f_i' obtained from least-squares fitting the experimental Dingle temperatures to Eq. (14) for vacancies and SFT.

| | Vacancies | | SFT | |
	R_5	R_6	R_5	R_6
f_1'	$0.111\,543 \times 10^{-11}$	$0.131\,603 \times 10^{-11}$	$0.462\,894 \times 10^{-12}$	$0.114\,957 \times 10^{-11}$
f_2'	$0.746\,161 \times 10^{-12}$	$0.835\,370 \times 10^{-12}$	$0.231\,298 \times 10^{-12}$	$0.542\,682 \times 10^{-12}$
f_3'	$0.240\,497 \times 10^{-12}$	$0.314\,334 \times 10^{-12}$	$0.108\,203 \times 10^{-12}$	$0.358\,432 \times 10^{-12}$
f_4'	$0.280\,059 \times 10^{-13}$	$0.774\,251 \times 10^{-13}$	$0.481\,094 \times 10^{-13}$	$0.212\,893 \times 10^{-12}$
f_5'	$0.503\,147 \times 10^{-13}$	$0.685\,172 \times 10^{-13}$	$0.319\,271 \times 10^{-13}$	$0.935\,825 \times 10^{-13}$
f_6'	0.0	$0.874\,037 \times 10^{-14}$	0.0	$0.291\,818 \times 10^{-13}$
rms error	2.18%	2.15%	8.48%	8.39%

is only about 30%, but the variation in the local lifetime $\tau(\hat{k})$ is found to be much larger, as much as a factor of 5, with the strongest scattering arising from the [100] region.

The local lifetime map for SFT in Au2A calculated with a six-term fit is shown in Fig. 9. The scattering pattern is significantly different from that for vacancies. The scattering rate in the [100] region is nearly unchanged, while the rate on the neck regions is increased sharply. On other regions of the surface, the scattering rate is generally smaller for SFT, consistent with the decreasing resistivity for SFT. Inversion of SFT data using a representation with cubic symmetry assumes all allowed SFT orientations are equally populated. The $\tau(\hat{k})$ deduced are averages over an ensemble of real space cyclotron orbits whose properties fluctuate depending on how the SFT are distributed in space.

By comparing Figs. 9 and 5 one finds that the conduction electrons on regions with a larger Fermi radius k_F tend to scatter more strongly

from the SFT. This behavior is easily understood since regions of the Fermi surface that are closer to the Brillouin-zone boundary are expected to be more strain sensitive. A similar conclusion is reached from the observed effect of dislocations in copper on the lifetime anisotropy.[12]

V. DISCUSSION AND CONCLUSION

In Table IV we compare the dHvA scattering rates from several types of point defects in gold. A theoretical estimate of the scattering rates from vacancies has been made[46] in copper and these values are listed for comparison. The first two columns of the table are Dingle temperatures per at.% point defects for $\langle 111 \rangle$ neck and belly orbits, respectively. The scattering anisotropy ξ [defined as the ratio of the neck to belly scattering rate $(T_D)_N/(T_D)_B$], the valence differences ΔZ between the defect and the host atom, and the lattice parameter changes $\Delta a/a$ per at.% point defects are
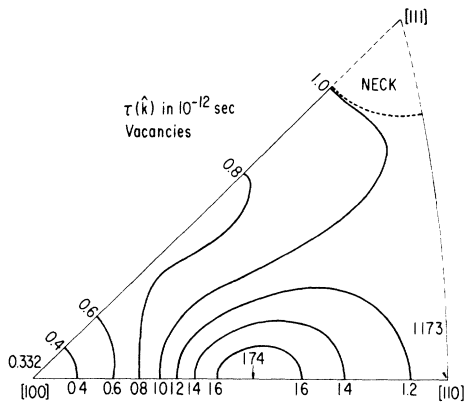

FIG. 8. Lifetime map shown on $\frac{1}{48}$ of the Fermi surface for sample Au2 calculated from Eq. (15).
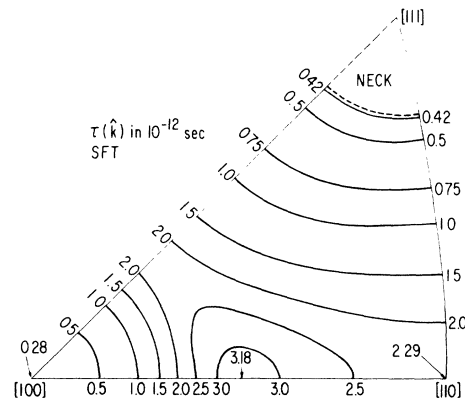

FIG. 9. Lifetime map shown on $\frac{1}{48}$ of the Fermi surface for sample Au2A calculated from Eq. (15).

TABLE IV. Comparison of point-defect scattering in gold.

	$(T_D)_N$ (°K/at.%)	$(T_D)_B$ (°K/at.%)	$\xi = \dfrac{(T_D)_N}{(T_D)_B}$	ΔZ	$\Delta a/a$ (1 at.%)
Au(Ag)[a]	2.8	9.3	0.30	0	−0.006%[b]
Au(Cu)[a]	4.5	10.1	0.45	0	−0.085%[b]
Au(Zn)[a]	25	39	0.63	1	−0.04%[b]
Au(Ga)[c]	78	107	0.73	2	−0.018%[b]
Au(vac.)	55	52	≳1.0	−1	−0.18%[d]
Cu(vac.)[e]	40~45	~40	≳1.0	−1	−0.11%[d]

[a] Reference 47.   [d] Reference 50.
[b] Reference 49.   [e] Reference 46.
[c] Reference 48.

also given. Since the neck scattering in a noble
metal is very sensitive to strain produced by the
lattice distortion surrounding a defect,[12] the scat-
tering anisotropy ξ is a sensitive indicator of the
lattice distortion effect. It is apparent from Table
IV that for point defects the scattering anisotropy
ξ depends not only on the strength of the potential
scattering associated with defect itself, but also
on the lattice distortion surrounding each defect.
The scattering from the vacancies, which have a
ΔZ of −1, is stronger than that from a system like
Au(Zn), which has also a valence difference of 1
(but opposite sign).

To date, conduction electron scattering from
four (structural) defect systems has been studied
using the dHvA effect. These systems are the
following: edge dislocations in copper produced
by pure bending,[10,12] dislocation loops in copper
generated by neutron irradiation,[13] and vacancies
and SFT in gold. For comparison we have listed
the experimental results in Table V. Two param-
eters are given in the table: one is the ratio of the
dHvA scattering rate to the scattering rate deter-
mined from the resistivity measurement $(1/\tau)_{dHvA}/$
$(1/\tau)_\rho$ and the other is the scattering anisotropy
ξ. The first ratio $(1/\tau)_{dHvA}/(1/\tau)_\rho$ measures the
significance of the small-angle scattering, e.g.,
that arising from the defect strain field. This ratio
is 10^3–10^4 for edge dislocations in copper, and
only 3–7 for dislocation loops. This shows the
dominance of small-angle scattering from the

TABLE V. Comparison of results among defect
systems.

Defect system	$(1/\tau)_{dHvA}/(1/\tau)_\rho$	ξ
Edge dislocations in Cu	10^3–10^4	4–5
Dislocation loops in Cu	3–7	5.5
Vacancies in Au	1.5~2	1.0
SFT in Au	>30	3.4
Impurities in noble metals	~1	≤1

long-range $(1/r)$ strain field of edge dislocations[12]
in the one case, and the weaker $(1/r^2)$ long-range
strain field for the loops in the other. $(1/\tau)_{dHvA}/$
$(1/\tau)_\rho$ is over 30 for SFT in gold, and 1.5 to 2 for
vacancies. This indicates that the strain field of
stacking-fault tetrahedra has a strong effect. For
substitutional impurities this ratio is about 1, in-
dicating no significant strain effect is involved.[51,52]

The generally large values of ξ for the structural
defect systems shown in Table V are caused by the
large strain fields associated with these defects.
However, ξ is apparently also sensitive to the geo-
metry of the defect, as evidenced by the fact that ξ
does not simply follow $(1/\tau)_{dHvA}/(1/\tau)_\rho$. One gen-
eral trend discernible from the table is that ξ in-
creases as the symmetry of the defect system de-
creases, i.e., the point-group symmetry of the
crystal-plus-defect system decreases in the order
vacancies, SFT, and dislocations. As shown in
Table V, ξ increases in precisely the same order.

We feel there is a great deal more information
available from the anisotropy of the lifetime; how-
ever, extracting this information will require theo-
retical models which can be used to interpret the
data. The interpretation of scattering lifetimes
from impurities is an example of what can be ac-
complished with strong interplay between theory
and experiment. The fitting of experimental scat-
tering data, using phase shifts of the KKR band-
structure scheme as fitting parameters, has led
to a new understanding of the electron impurity
interaction, based on angular momentum decom-
position of the scattering and screening.[42,53,54] Un-
fortunately, the KKR model used for the impurity
work does not allow for any lattice distortion
around the impurity and therefore cannot be used
directly for defect systems. The phase smearing
approach has been successful in explaining some
of the measured Dingle temperatures,[12,55] but is
not widely applicable. If microscopic models deal-
ing with scattering from distorted crystals can be
developed, the detailed information contained in

dHvA lifetime anisotropies can be put to maximum use.

Even in the absence of such theories, dHvA experiments are still useful for studying defect systems. The measured Dingle temperatures are sensitive to the strain field induced by the defect as well as the defect itself; the resistivity is primarily sensitive only to the defect itself. However, the dHvA effect offers more information than the resistivity, since lifetimes for different cyclotron orbits may be measured independently. As shown by the data for vacancies and SFT, the lifetimes of different orbits may respond quite differently to a change in the defect character. In effect, the lifetime for each orbit gives an independent picture of the annealing process.

The dHvA effect can be applied to study defects in many of the materials which are currently studied only by resistivity measurements. The dynamics of defect migration and transformation can be observed through annealing studies as a function of time or temperature. Such experiments could be useful in understanding the complex changes which occur in the annealing of radiation damaged materials. For the near future, further experiments on defects in noble metals and other well characterized systems (e.g., Pt and Al) seem most useful. These will provide the simplest cases for testing the effectiveness of the dHvA technique and for interpreting the results.

ACKNOWLEDGMENTS

*Based on work performed under the auspices of the U. S. ERDA.

†Present address: Solid State Div., Oak Ridge National Laboratory, Oak Ridge, Tenn. 37830.

[1]For example, J. E. Baurle and J. S. Koehler, Phys. Rev. 107, 1493 (1957); M. de Jong and J. S. Koehler, ibid. 129, 49 (1963).

[2]J. Silcox and P. B. Hirsch, Philos. Mag. 4, 1356 (1959).

[3]J. A. Ytterhus and R. W. Balluffi, Philos. Mag. 11, 707 (1965).

[4]R. W. Siegel, Philos. Mag. 13, 337 (1966).

[5]A. Yoshinako, Y. Shimomura, M. Kiritani, S. Yoshida, Jpn. J. Appl. Phys. 7, 709 (1968).

[6]T. M. Hall, A. N. Goland, K. C. Jain, and R. W. Siegel, Phys. Rev. B 12, 1613 (1975).

[7]B. Lengeler, Philos. Mag. 34, 259 (1976).

[8]A. V. Gold, in Solid State Physics, Vol. 1, Electrons in Metals, edited by J. F. Cochran and R. R. Haering (Gordon and Breach, New York, 1968), p. 39.

[9]M. Springford, Adv. Phys. 20, 493 (1971).

[10]D. W. Terwilliger and R. J. Higgins, Phys. Lett. A 31, 316 (1970); Phys. Rev. B 7, 667 (1973).

[11]P. T. Coleridge and B. R. Watts, Philos. Mag. 24, 1163 (1971); B. R. Watts, ibid. 24, 1151 (1971).

[12]Y. K. Chang and R. J. Higgins, Phys. Rev. B 12, 4261 (1975).

[13]Y. K. Chang, A. J. Arko, G. W. Crabtree, J. B. Ketterson, L. R. Windmiller, R. J. Higgins, and F. W. Young, Jr., in Fundamental Aspects of Radiation Damage in Metals, edited by M. T. Robinson and F. W. Young, Jr. (National Technical Information Service, Springfield, Va., 1976), p. 846.

[14]Y. K. Chang, G. W. Crabtree, J. B. Ketterson, and L. R. Windmiller, Bull. Am. Phys. Soc. 20, 353 (1975).

[15]Y. K. Chang, G. W. Crabtree, and J. B. Ketterson, Proceedings of the International Conference on Atomic Defects in Metals (Argonne, Ill., 1976) (unpublished).

[16]B. Lengeler and W. Uelhoff, Phys. Lett. A 53, 139 (1975); and in Ref. 15.

[17]D. Shoenberg and P. J. Stiles, Proc. R. Soc. A 281, 62 (1964).

[18]R. W. Stark and L. R. Windmiller, Cryogenics 8, 272 (1968).

[19]L. R. Windmiller and J. B. Ketterson, Rev. Sci. Instrum. 39, 1672 (1968).

[20]J. J. Jackson, in Lattice Defects in Quenched Metals, edited by R. M. J. Cotterill, M. Doyama, J. J. Jackson, and M. Meshii (Academic, New York, 1965), p. 479.

[21]D. Jeannotte and E. S. Machlin, Philos. Mag. 8, 1835 (1963).

[22]G. W. Crabtree, J. B. Ketterson, and L. R. Windmiller, J. Low Temp. Phys. 26, 755 (1977).

[23]D. Shoenberg, Phys. Kondens. Mater. 9, 1 (1969).

[24]S. P. Hornfeldt, J. B. Ketterson, and L. R. Windmiller, J. Phys. E 6, 265 (1973).

[25]F. M. Mueller, Phys. Rev. 148, 636 (1966).

[26]F. M. Mueller and M. G. Priestley, Phys. Rev. 148, 638 (1966).

[27]J. B. Ketterson, L. R. Windmiller, S. Hornfeldt, and F. M. Mueller, Solid State Commun. 6, 851 (1968).

[28]A. J. Arko and F. M. Mueller, Phys. Rev. Lett. 29, 1515 (1972).

[29]D. J. Roaf, Phil. Trans. Soc. Lond. A 255, 135 (1962).

[30]M. R. Halse, Phil. Trans. R. Soc. Lond. A 265, 596 (1969).

[31]J. B. Ketterson, F. M. Mueller, and L. R. Windmiller, Phys. Rev. 186, 656 (1969).

[32]B. Bosacchi, J. B. Ketterson, and L. R. Windmiller, Phys. Rev. B 2, 3025 (1970).

[33]B. Bosacchi, J. B. Ketterson, and L. R. Windmiller, Phys. Rev. B 4, 1197 (1971).

[34]B. Bosacchi, J. B. Ketterson, and L. R. Windmiller, Phys. Rev. B 5, 3816 (1972).

[35]B. Segall and F. J. Ham, Methods Comput. Phys. 8, 251 (1968).

[36]M. J. G. Lee, Phys. Rev. 178, 953 (1969).

[37]M. J. G. Lee, Phys. Rev. 187, 901 (1969).

[38]M. J. G. Lee, Phys. Rev. Lett. **25**, 28 (1970).

[39]J. C. Shaw, J. B. Ketterson, and L. R. Windmiller, Phys. Rev. B **5**, 3894 (1972).

[40]P. T. Coleridge, J. Phys. F **2**, 1016 (1972).

[41]P. T. Coleridge, Phys. Rev. B **7**, 3508 (1973).

[42]P. T. Coleridge, N. A. W. Holzwarth, and M. J. G. Lee, Phys. Rev. B **10**, 1213 (1974).

[43]J. F. Koch, in Ref. 8, p. 253.

[44]J. F. Koch and R. E. Doezema, Phys. Rev. Lett. **24**, 507 (1970).

[45]R. E. Doezema and J. F. Koch, Phys. Rev. B **6**, 2071 (1972).

[46]W. Hehl and E. Mann, Phys. Status Solidi B **78**, 271 (1971).

[47]D. H. Lowndes, K. M. Miller, R. G. Paulsen, and M. Springford, Proc. R. Soc. A **331**, 497 (1973).

[48]D. H. Dye, J. B. Ketterson, D. H. Lowndes, G. W. Crabtree, and L. R. Windmiller, J. Low Temp. Phys. **26**, 945 (1977).

[49]W. B. Pearson, *Handbook of Lattice Spacings and Structure of Metals* (Cambridge U.P., Cambridge, England, 1969).

[50]M. W. Thompson, *Defects and Radiation Damage in Metals* (Cambridge U.P., Cambridge, England, 1969).

[51]P. T. Coleridge, Philos. Mag. **26**, 573 (1972); **27**, 1495 (1973).

[52]B. R. Watts, J. Phys. F **3**, 1345 (1973).

[53]N. A. W. Holzwarth, Phys. Rev. B **11**, 3718 (1975).

[54]M. J. G. Lee, N. A. W. Holzwarth, and P. T. Coleridge, Phys. Rev. B **13**, 3249 (1976).

[55]B. R. Watts, J. Phys. F **4**, 1371 (1974).